Experimental characterisation of dynamic stall of the FFA-W3-211 wind turbine airfoil

Simone Chellini[1], Delphine De Tavernier[1], and Dominic von Terzi[1]

[1]Faculty of Aerospace Engineering, Delft University of Technology, 2629HS Delft, The Netherlands

Correspondence: Simone Chellini (s.chellini@tudelft.nl)

Abstract. In this work, an experimental campaign was carried out to determine both the static and dynamic aerodynamic properties of the FFA-W3-211 airfoil. This airfoil is widely used in the wind energy community as part of IEA reference wind turbine designs, but is lacking experimental data for design, simulation tool validation and dynamic stall modelling purposes. The airfoil model was designed and manufactured for testing in the Low Speed, Low Turbulence wind tunnel at TU
5   Delft. The airfoil was tested statically for Reynolds numbers ranging from $Re_c = 5 \times 10^5$ to $Re_c = 3.5 \times 10^6$ and dynamically for up to $Re_c = 2 \times 10^6$, encompassing steady, unsteady and highly unsteady aerodynamic behaviour. Data were acquired through pressure measurements at the surface of the airfoil and in the wake, as well as by using thermal cameras. The static results highlighted a strong dependence of the lift and drag polars on the Reynolds number and a change in trends around $Re_c = 2 \times 10^6$. The suspected presence of laminar separation bubbles for the lower Reynolds numbers could explain this
10   fundamental change in flow behaviour. The dynamic behaviour was studied at high positive angles of attack, high negative angles of attack and within the linear region of the polar around the zero-lift angle. The positive region is governed by the lack of a leading-edge vortex. This is in contrast to the negative region of the polars where the effects of a vortex appearing close to the leading edge dominate. The sensitivity of the results to reduced frequency, amplitude, and Reynolds number is discussed. Overall, for the FFA-W3-211 airfoil, it is recommended to use experimental data of $Re_c = 2 \times 10^6$ or above to capture the
15   correct physical (static and dynamic) trends relevant for larger wind turbine blades. For dynamic stall model tuning, it may also be important to consider the significant change in behavior between positive and negative stall angles.

1 Introduction

Wind turbines have seen a substantial increase in rotor diameters, as testified in the latest available reference wind turbine (RWT) of the International Energy Agency (IEA), the *IEA 22MW RWT*, which features a rotor diameter of $D = 284m$ and a
20   hub height of $h = 170m$ (Zahle et al., 2024). Such a large wind turbine is prone to experiencing significant time-varying inflow conditions along the blades due to, among others, wind shear, turbulence, aeroelastic deflections and yaw misalignment. The force enhancement due to dynamic oscillations is responsible for design loading conditions that are often difficult to quantify and affect the blade's lifespan and overall turbine performance. For a given wind condition, dynamic stall can be one of the largest sources of load uncertainty for such wind turbines. This is corroborated by observations that, in simulations of large
25   rotors, the choice of the dynamic stall model and its airfoil-dependent parameters can lead to qualitatively very different loads

assessments (see Stettner et al., 2016, for example). For this reason, airfoils that undergo dynamic stall effects have generated renewed research interest.

Dynamic stall has long been observed as design driving in applications and, therefore, has been often discussed in the literature, see Ham (1967), Leishman (2002), Gardner et al. (2023) and the citations therein to name only a few. While it is important to bear in mind that the mechanisms of dynamic stall vary depending on the airfoil profile and flow conditions, a generalisation of the phenomenon could be described as in the following: The boundary layer separation on the airfoil is delayed above the equivalent static stall angle, after which a *dynamic stall vortex* (DSV) is shed from the airfoil's suction side. This process causes a temporary increase in lift exceeding the maximum steady-state equivalent. A nose-down pitching moment and boundary layer reattachment complete the cycle that forms a dynamic stall hysteresis loop. The loop varies greatly in magnitude depending on the oscillating conditions.

Many experiments have investigated different aspects of dynamic stall, including the effect of add-ons. In De Tavernier et al. (2021), the effect of vortex generators (VGs) was demonstrated in unsteady conditions for the DU17DBD25, an airfoil specifically designed for a sub-MegaWatt vertical-axis wind turbine. The results were acquired for a chord-based Reynolds number of $Re_c = 10^6$, showing that wind turbine blades would benefit from passive VGs installations for flow control. In Rainbird et al. (2015), the effects of virtual camber were investigated experimentally for the symmetric NACA0018 airfoil. The experimental campaign was carried out in the Parkinson blockage tolerant tunnel at Imperial College for $Re_c = 3 \times 10^5$. The polars were compared with a CFD study to highlight that consideration of the airfoil's curvature should be included when comparing results from BEM codes with CFD. The NACA 23012 was tested dynamically at $Re_c = 1.5 \times 10^6$ in Leishman (1990). The experiment was carried out in the Handley-Page low-speed wind tunnel at the University of Glasgow, where data for the $c = 0.55m$ wing was acquired via 30 pressure taps, highlighting the increasing stall abruptness with increasing Reynolds numbers and the characteristic lift increase associated with the nose-up motion.

Experimental characterisation of the dynamic stall phenomena can be challenging, particularly when combining medium-to-high Reynolds numbers with unsteady reduced frequencies. In the work of Carta (1974) and McAlister et al. (1978), dynamic stall was analysed for an airfoil pitching sinusoidally. While simplified, the sinusoidal case provides a good testing benchmark replicating helicopter or wind turbine blades. Patterson and Lorber (1990) compared the results of a medium-level Reynolds number experiment carried out for $2 \times 10^6 < Re < 4 \times 10^6$ for a supercritical airfoil, the $Sikorsky\ SSC-A09$ with two computational methods. The review in McCroskey (1982) provides background for airfoils undergoing transonic flow conditions dynamically.

Recently, dynamic stall was studied for a NACA0021 airfoil in Kiefer et al. (2022) at high Reynolds number flows. The experiment was conducted in a pressurised facility where high Reynolds numbers close to full-scale conditions can be reproduced. Thanks to a low free-stream velocity, the facility allows the pure effects of the Reynolds number to be isolated, with no transonic effects due to the low Mach number. Overall, combining high Reynolds numbers with dynamic stall testing was proven to be difficult. The literature has repeatedly shown the need for a deeper understanding of Reynolds numbers effects for wind turbine airfoils, with a special focus on the more complex transient case, which heavily impacts the wind turbine design (Kiefer et al., 2022).

Dynamic stall has been thoroughly investigated through simulations in the past, often trading off the Reynolds number and reduced frequency. The work of Boye and Xie (2022) investigates the effects of high reduced frequencies for a NACA0012 airfoil, albeit for chord-based Reynolds numbers of only $Re_c = 135.000$. More studies were conducted to analyse the pitching of the NACA0012, all for low Reynolds numbers in Tuncer et al. (1990), Choudhuri and Knight (1996) and Gharali and Johnson (2013). While the airfoil is often considered a wind turbine benchmark, the low thickness and lack of a cambered profile make it unsuitable for wind turbines. Gardner et al. (2023) recently highlighted the renewed interest in dynamic stall, reviewing relevant work in the field. The authors provide an extensive overview of the experimental state-of-the-art, as well as future research directions and integration with computational studies. The review highlights the need for experiments replicating real-life conditions, both for rotor and fixed-wing aerodynamics. Time-resolved force and pressure data are required to fully understand the full temporal analysis of the phenomena. Considerations regarding transition, reverse flow and dynamic stall control are also introduced, reviewing passive and active dynamic stall control devices. The review shows the impact of separation, blade-vortex interactions and shock-airfoil interactions on safer and more efficient rotating wing systems.

Dynamic stall predictions rely on simulation data models, such as the Leishman and Beddoes (1989) model, that are not developed specifically for wind-turbine tip-airfoils characterised by a thickness of $\approx 20\%$ (Boutet et al., 2020) and high camber. The importance of the Beddoes-Leishman (BL) model and its correct implementation is shown in Melani et al. (2024), highlighting the role of the experimental data in calibrating dynamic stall models correctly. Initial results from Chellini et al. (2024) show the consistent failure of the Beddoes-Leishman model in capturing the transient aerodynamic behaviour, particularly at negative angles of attack, where most dynamic stall models lack experimental calibrations. For instance, despite being based on symmetric airfoil data, the BL model fails to replicate the experimental separation and load enhancement associated with negative angles of attack. In wind turbines, the model is widely adopted in popular tools such as OpenFAST, leading to inaccurate load reconstructions (Chellini et al., 2024). Other empirical and semi-empirical models such as the models of Onera (McAlister et al., 1984), Oye (Øye, 1991) and Snel (Snel, 1997) could be calibrated similarly to the BL model requiring the corresponding airfoil data.

The *IEA 22MW RWT* and its predecessor, the *IEA 15MW RWT* (Gaertner et al., 2020), employ airfoils from the *FFA* family at the outboard sections of their blades with different thicknesses depending on their span location, for which the dynamic stall characteristics are not yet fully established. To understand the physical features of dynamic stall on relevant wind turbine airfoils, this work presents the results of the *FFA-W3-211* airfoil tested in static and dynamic conditions. The experiment was carried out for a range of static and dynamic inflow angles and steady to highly unsteady reduced frequencies, chosen to characterise three distinct flow regions in the negative, linear and positive regions of the polars.

1.1 Objective and paper structure

This work presents experimental data for the FFA-W3-211 airfoil, quantifying the static and dynamic aerodynamic behaviour. The primary objective is to investigate how the combination of reduced frequency and Reynolds number impacts the airfoil's dynamic loading. Analysis is carried out to understand the driving factors affecting the flow physics around the airfoil. Firstly,

the experimental post-processing procedure is introduced. This is followed by validating the newly acquired data against existing experimental results in §3.1. The analysis of the static and dynamic loads follows in §3.2. The analysis is divided into Reynolds number, reduced frequency, oscillating frequency and amplitude effects, isolating the experimental and relevant flow physics parameters.
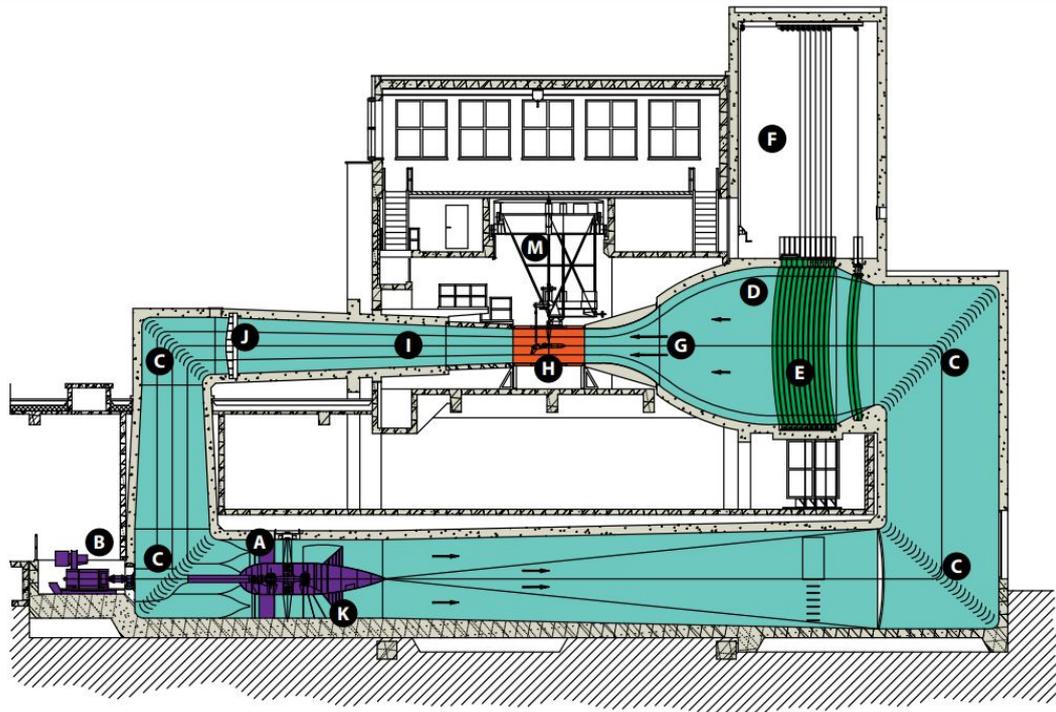
2 Experimental set-up

2.1 Wind tunnel facility

The experimental campaign is carried out in the *Low-Speed Low-Turbulence wind tunnel* (LTT) of Delft University of Technology, a closed-section recirculating wind tunnel. The facility features changeable octagonal testing sections, with a width of 1.80m, length of 2.60m and height of 1.25m. The octagonal testing section returns a cross-sectional area of $A_{ltt} = 2.07m^2$. Each testing section is equipped with a mechanically actuated turntable flush to the tunnel's top and bottom walls, which allows the airfoil's angle of attack to be set with a precision of $\pm 0.1°$. The turbulence level varies from 0.015% at $20m/s$ to 0.07% at $75m/s$ due to the large contraction ratio of 17.83. The six-bladed fan is powered by a 525 kW DC motor, returning a free-stream velocity up to $U_\infty = 120ms^{-1}$, and Reynolds numbers up to $Re_c = 3.5 \times 10^6$ depending on the airfoil's chord. More details can be found in Delft (2017). The full diagram of the facility can be found in Fig. 1.

2.2 Airfoil model

An FFA-W3-211 airfoil model with a maximum thickness of 21.1% chord (Fig. 2) is manufactured from carbon fibre composite. The airfoil model has a chord length of $c = 600$ mm and a length of $h = 1246$ mm to span the LTT test-section height, resulting in an aspect ratio $AR \approx 2$, in line with previous airfoils tested in this facility (e.g., Baldacchino et al., 2018; Timmer and Van Rooij, 2003; Llorente et al., 2014). The carbon fibre thickness varies along the airfoil's span, with local refinements around the leading edge. Due to the high skin thickness, with a minimum of $t = 1.7mm$ and a maximum of $t = 6mm$ at the leading edge, no visual surface deformation was observed during the experiment. The trailing edge thickness is measured as 1.7 mm.

A total of 93 pressure taps, refined around the leading edge, with a diameter of 0.4 mm, are distributed on the airfoil skin. The taps distribution is angled at $\approx 15°$ to reduce any potential boundary layer disruption between the orifices. Each pressure tap is connected to an ≈ 2.7 m long tube, which exits the airfoil model through a lower aperture located at around $x/c = 0.5$. Importantly, this represents a limitation for the airfoil's oscillating amplitude, which can operate safely between $-25° < \alpha < 25°$. The airfoil model was polished to a mirror-finish texture, and the flow transition from laminar to turbulent was verified with thermal cameras to ensure that no model imperfection provoked early transition, as shown in Fig. 3, and confirm sufficient 2D uniformity of the model. A comparison between $Re_c = 1.0 \times 10^6$ and $Re_c = 3.5 \times 10^6$ is visible in Fig. 3. At the top of Fig. 3, an irregularity is visible, which is caused by light reflections from the wind tunnel walls and a small defect in the surface (only visible at the higher Reynolds number). Based on the defect being ocated far away from the pressure orifices and by inspecting

Figure 1. Diagram of the low-speed, low-turbulence wind tunnel at TU Delft. The flow reaches the testing section from right to left.

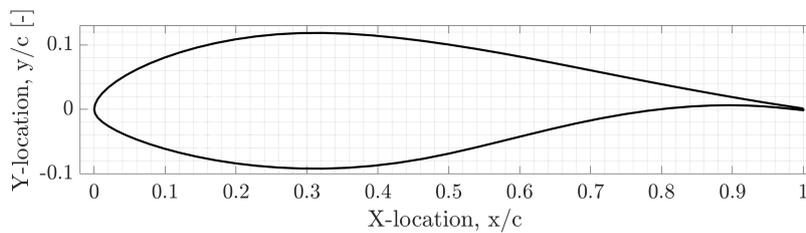|			
A Fan and straighteners	**E** Anti-turbulence screens	**I** Diffuser
B Motor	**F** Screen store room	**J** Security screen
C Corner Vanes	**G** Contraction	**K** Spider web
D Settling chamber	**H** Exchangeable test section	**M** Six-component balance

Figure 2. Cross section of the FFA-W3-211 airfoil. The cambered airfoil has a thickness of 21.1 %.

drag measurements derived from pressure measurements in the wake (not shown in this paper), it was concluded that this artifact is unlikely to have influenced any of the measurements reported here.
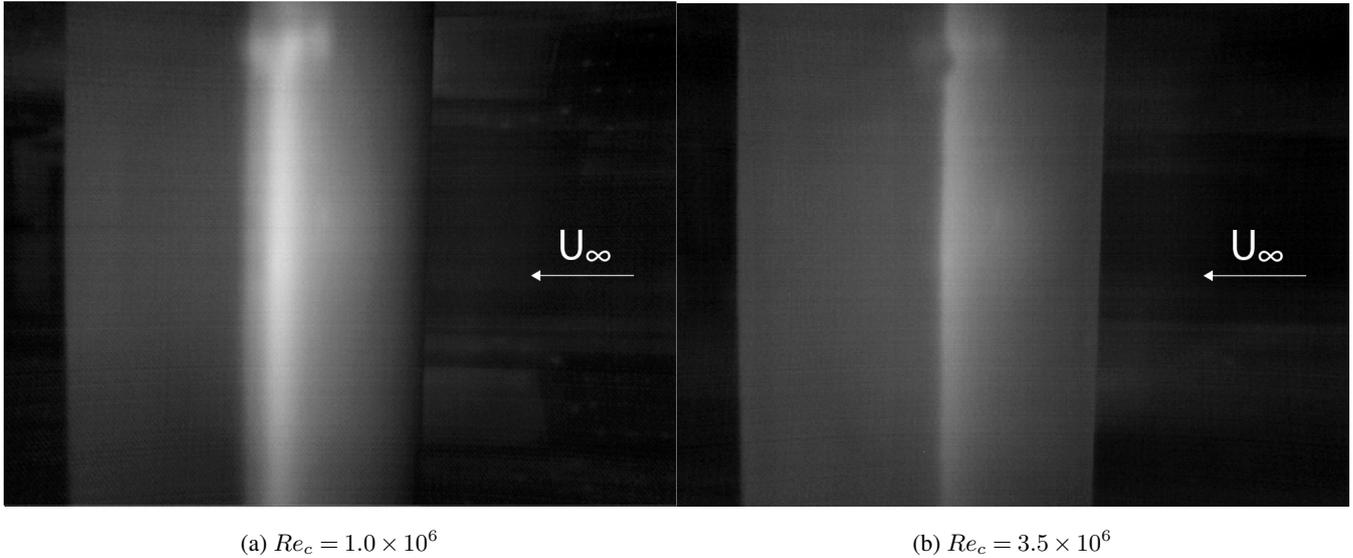
(a) $Re_c = 1.0 \times 10^6$ (b) $Re_c = 3.5 \times 10^6$

Figure 3. Qualitative transition location on the airfoil's suction side for $\alpha = 0°$. The upper reflection does not affect the airfoil's wake-derived drag coefficient and surface pressure-derived lift coefficient.

2.3 Data acquisition

2.3.1 Static measurements

The 2D flow data was acquired through the 93 pressure taps, connected to the pressure scanner through four adapters. The pressure measurements at the leading and trailing edges were split into two channels for redundancy. The pressure scanner was also used to acquire the total and static pressure in the wind tunnel. In static cases, a wake rake is used to quantify the loss of momentum in the wake. This comprises 67 pressure tubes and 16 static tubes over a length of 504 mm. The pressure rake automatically centres the wake and traverses along the spanwise direction for each acquisition to average potential three-dimensional flow effects. When the rake can no longer capture the airfoil's turbulent wake, pressure drag is used instead. Data are sampled at a frequency of $5Hz$. A $2mm$ gap is found between the wind tunnel walls and the wing on each side. The gaps were sealed with tape during the static measurements in order to minimise the loss of momentum from the lower aperture, through which the pressure tubes exit, and the 3D finite wing effects.

The airfoil section is rotated using the wind tunnel turntable for the static polars acquisition around its quarter-chord line. The static polars are acquired for angles of attack of $-20° < \alpha < 20°$. Local refinements are carried out to characterise the stall region and the design lift-to-drag ratio. The static experiment is carried out for $5 \times 10^5 < Re_c < 3.5 \times 10^6$. Therefore, the equivalent Mach number for the highest Reynolds number case is evaluated as $M = 0.25$, and compressibility effects can be assumed negligible in the analysis. To avoid any impurities on the airfoil's surface, that may lead to early boundary layer transition, the model was regularly cleaned to guarantee a clean dust-free surface.

The lower pressure distribution $C_{p,l}$ and upper pressure distributions $C_{p,u}$, obtained from the pressure taps on the airfoil's surface, are integrated to determine the normal coefficient (Eq. (1)), where the prime indicates, here and in the following, uncorrected values. c is the airfoil chord.

$$C_n' = \int_0^1 (C_{p,l} - C_{p,u}) \, d\left(\frac{x}{c}\right) \tag{1}$$

The drag coefficient is obtained through the wake rake pressure readings according to Eq. (2), where $C_{p,t}$ is the total pressure and $C_{p,s}$ refers to the static pressure

$$C_d' = \frac{2}{c} \int_{\text{wake}} \sqrt{C_{p,t} - C_{p,s}} \left(1 - \sqrt{C_{p,t}}\right) dy \tag{2}$$

The normal and drag coefficients and the angle of attack (α) are used to quantify the 2D lift in Eq. (3).

$$C_n' = C_l' \cos(\alpha) + C_d \sin(\alpha) \quad C_l' = \frac{C_n'}{\cos(\alpha)} - C_d' \tan(\alpha) \tag{3}$$

2.3.2 Dynamic measurements

The wing model's shaft was connected to a UniMotion PNCE 40 BS 1610 linear actuator for dynamic testing purposes. The actuator's extrusion is connected to the airfoil's steel shaft to couple the linear and pitching motions, and its extrusion is controlled through a LabVIEW script. An angular encoder is coupled to the airfoil's shaft, providing the real-time angle of attack reading. More details regarding the setup can be found in De Tavernier et al. (2021). Data is sampled from the wing's pressure taps with the same methodology described in the previous section, with a frequency of $300Hz$. The dynamic polars were acquired by pitching the airfoil section around its quarter-chord line.

Due to the aerodynamic loads acting on the airfoil model, airfoil pitching system and its connection, the set-up was experiencing some aeroelastic response. To cope with this, the actuator calibration (linking the actuator motion to the airfoil angle of attack) was performed independently for different Reynolds numbers, to guarantee accurate angles of attack.

A representative, yet simplified, oscillation case for a wind turbine airfoil is defined by a simple sinusoidal motion, described in Eq. (4) as

$$\alpha(t) = \alpha_0 + A sin(2\pi f t), \tag{4}$$

where α_0 is the initial mean angle of attack, A is the oscillating amplitude, and f is the oscillating frequency in Hertz. The actuator was controlled through a LabVIEW program.

The frequency from Eq. (4) also sets the reduced frequency, k, which is defined here as

$$k = \frac{\pi c f}{U_\infty}, \tag{5}$$

Figure 4. Experimental setup details. The top left image shows the testing section geometry, with the wake rake behind the airfoil. The linear actuator mechanism is shown in the top right image. The testing section installed in the wind tunnel is shown in the bottom left image, without the covering panels for visibility purposes. The airfoil model (with sealed gaps between the wind tunnel walls and airfoil model) is shown in the bottom right image, with the thermal cameras installed at the airfoil's midspan, for $x/c = 50\%$

where c is the airfoil's chord and U_∞ is the free-stream velocity. This non-dimensional parameter describes the degree of unsteadiness in oscillation. Three separate unsteady regimes are identified in Corke and Thomas (2015). The flow field can be considered unsteady for $0.05 \leq k \leq 0.2$, and highly unsteady for $k \geq 0.2$. Below 0.05, the unsteady effects may be assumed negligible and, therefore, the corresponding flow regime is commonly referred to as quasi-steady. To capture the three unsteady flow regimes, a comprehensive span of Reynolds numbers and reduced frequencies is acquired around the negative and positive stall regions and the linear region of the polars.

Together with the local pressure on the airfoil, the atmospheric and operational conditions were recorded through the wind tunnel measurement devices, highlighting a variation in the instantaneous free-stream readings due to the changing blockage in the wind tunnel. Data were acquired for 50 sinusoidal cycles.

Table 1. Dynamic experimental matrix. Each parameter is changed independently of the others, returning four independent degrees of freedom in the experimental matrix.

Reynolds number [/]	Frequency [Hz]	Amplitude [°]	Mean Angle [°]
$Re_c = 5 \times 10^5$	0.6	± 3	-9.4
$Re_c = 1 \times 10^6$	1.2	± 5	-1.4
$Re_c = 2 \times 10^6$	1.8	± 7	9.6
	2.4	± 9	
		± 11	

2.4 Measurement corrections

2.4.1 Static data corrections

The static raw pressure data are corrected using the wall-effects correction approach defined in Dalton (1971). This approach corrects for lift interference, wake blockage, solid blockage, and streamline curvature. Here, the uncorrected drag is used to correct for wake blockage, directly affecting the corrected lift coefficient. The wake blockage is defined in Eq. (6) as

$$w_b = C_D \frac{0.25h}{c} \frac{1 + 0.4M^2}{\beta^2} \tag{6}$$

where M is the Mach number, and the compressibility factor is defined as $\beta = \sqrt{1 - M'^2}$. The wind tunnel blockage factor, σ is defined as

$$\sigma = \frac{\pi^2}{48} \left(\frac{c}{h} \right)^2 \tag{7}$$

The angle of attack is corrected using Eq. (8)

$$\alpha = \alpha' + \frac{57.3\sigma}{2\pi\beta} (C_l' + 4C_m') \tag{8}$$

2.4.2 Dynamic data corrections

Due to the dynamic oscillations, retrieving drag readings from the wake rake became unreliable. As the drag coefficient is used to obtain the lift coefficient, it is not possible to convert normal and tangential coefficients to the lift coefficient.

An initial delay and amplitude loss are found between the pressure sampled at the skin of the airfoil and at the end of the pressure tubes. Considering the pressure tube length, width, and testing conditions, the pressure lag and attenuation are handled in the post-processing using the correction method from Bergh and Tijdeman (1965). The method was coded in the software tool PreMeSys V2.0, validated in De Tavernier et al. (2021) for dynamic airfoil testing. The corrected pressure values are then

9

Table 2. Variation in lift curve slope in the linear region of the polars due to mass outflow and 3D finite wing effects for different Reynolds numbers. The quantification is not taken into account when reporting the dynamic polars results.

	Sealed gap slope	Open gap slope	Difference
$Re_c = 5 \times 10^5$	0.1177	0.1141	-3.1%
$Re_c = 1.5 \times 10^6$	0.1185	0.1158	-2.3%
$Re_c = 2.5 \times 10^6$	0.1205	0.1183	-1.8%

translated into instantaneous forces on the airfoil by means of integration.

While a methodology concerning aerodynamic (static) corrections for the presence of the wind tunnel walls had been validated, evidence of dynamic wall corrections are yet to be found in the literature. Therefore, previous literature, such as Kiefer et al. (2022) and De Tavernier et al. (2021), displayed the dynamic polars in an uncorrected manner. To quantify the potential effect of reporting uncorrected dynamic data rather than corrected dynamic data, Fig. 5a is provided. This figure shows the differences between the corrected, uncorrected and a partially corrected static lift polar for $Re_c = 10^6$. There is good agreement between the fully and partially corrected data regarding the location and value of $C_{L_{max}}$ and pre-stall slope. However, after the stall angle is reached, the effects of wake blockage become predominant in the corrections, with the partially corrected data diverging from the fully corrected data as the angle of attack increases and accounting for almost 50% at $\alpha = 20°$. However, as the correction approach is not proven, it was decided not to correct the data for wall effects and report uncorrected data only.

When testing dynamically, the tape sealing the 2mm gap between the airfoil walls and the wind tunnel was removed. This introduces 3D finite wing effects and allows flow to exit the tunnel through the (small) gap on the lower side of the wind tunnel. At low angles of attack, the airfoil cross-section fully or partially covers the gap, limiting the loss of momentum. However, as the angle of attack increases, the gap is more exposed to the free-stream flow. The loss of momentum through the wind tunnel aperture was determined for the linear region of polars. The effect of the sealing tape was quantified for three static cases, for $Re_c = 5 \times 10^5, 1.5 \times 10^6, 2.5 \times 10^6$, of which one is shown for clarity in Fig. 5b. To quantify the effect, the linear slope (defined between $-6° < \alpha < 6°$) is reported in Tab. 2. The results show minor effects, with the difference in the pre-stall slope decreasing with increasing Reynolds numbers. This is due to the higher flow inertia that, for higher free-stream velocities, allows the suction of the wind tunnel cavity to be overcome. As the static stall angles are approached, the loss of momentum becomes more evident for low Reynolds numbers while still showing similar stall trends across all cases. While the differences are within a reasonable range, it is believed that no additional correction is needed.
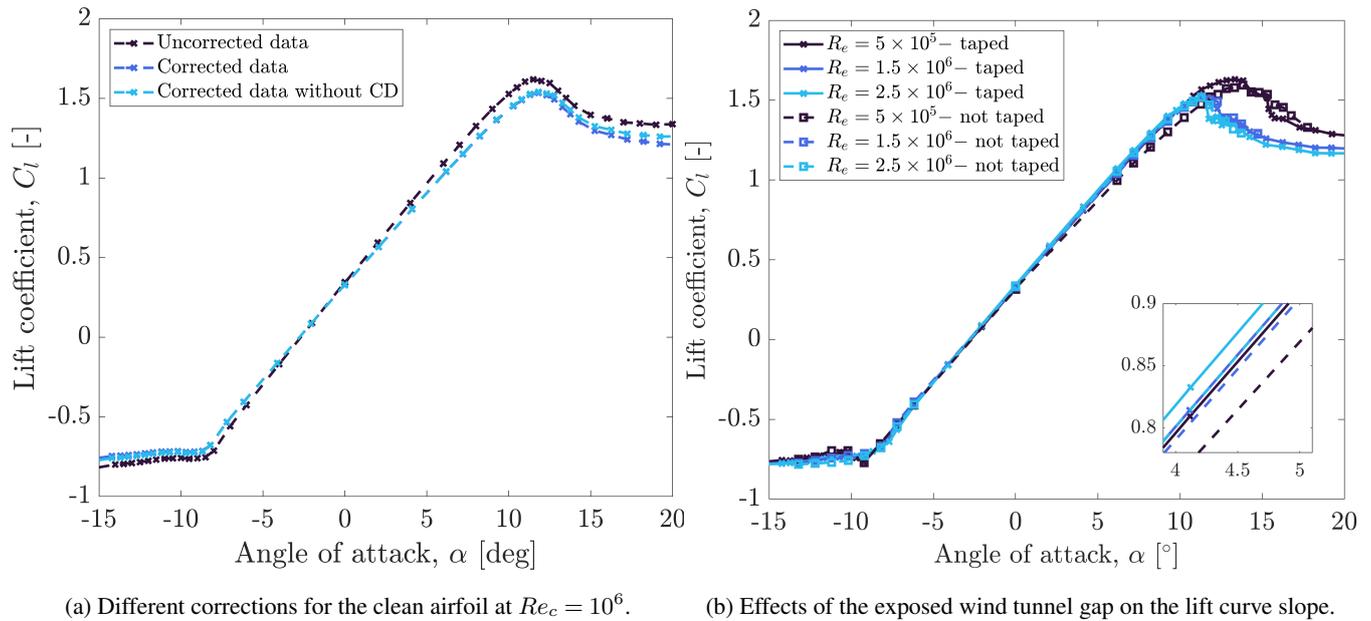
(a) Different corrections for the clean airfoil at $Re_c = 10^6$.

(b) Effects of the exposed wind tunnel gap on the lift curve slope.

Figure 5. Effects of the wake-blockage term and sealed wind-tunnel gap in the static lift coefficient curve
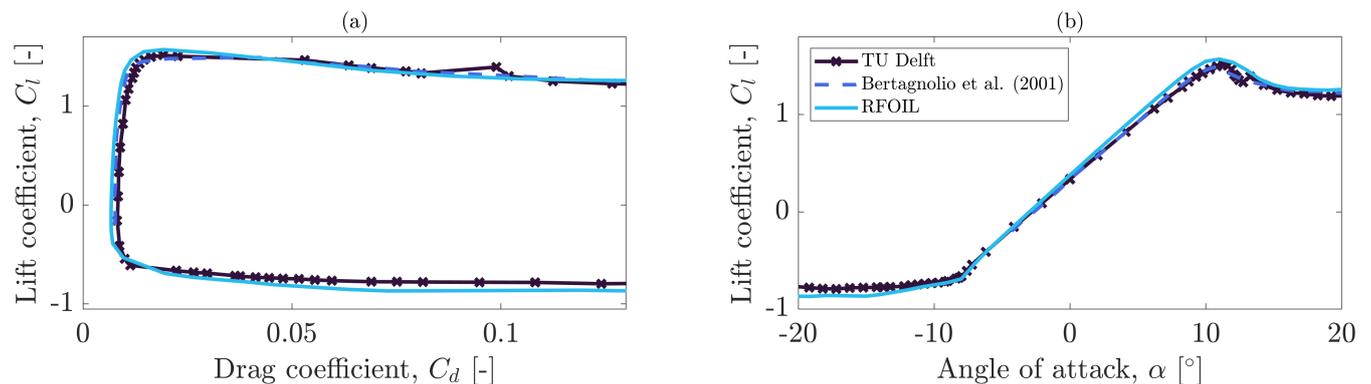

Figure 6. Clean polars comparison for the FFA-W3-211 airfoil for $Re_{e_c} = 1.8 \times 10^6$

3 Results and discussion

3.1 Validation

The static polar results are validated against existing experimental data. To the best of the authors' knowledge, the only experimental dataset available concerning the aerodynamic performance of the FFA-W3-211 airfoil is Bertagnolio et al. (2001). In their work, the FFA-W3-211 airfoil was tested for a chord-based Reynolds number of $Re_c = 1.8 \times 10^6$ in the low-speed wind tunnel L2000 at KTH. The experimental facility has a two by two metres section, with a turbulence intensity of 0.15%. The
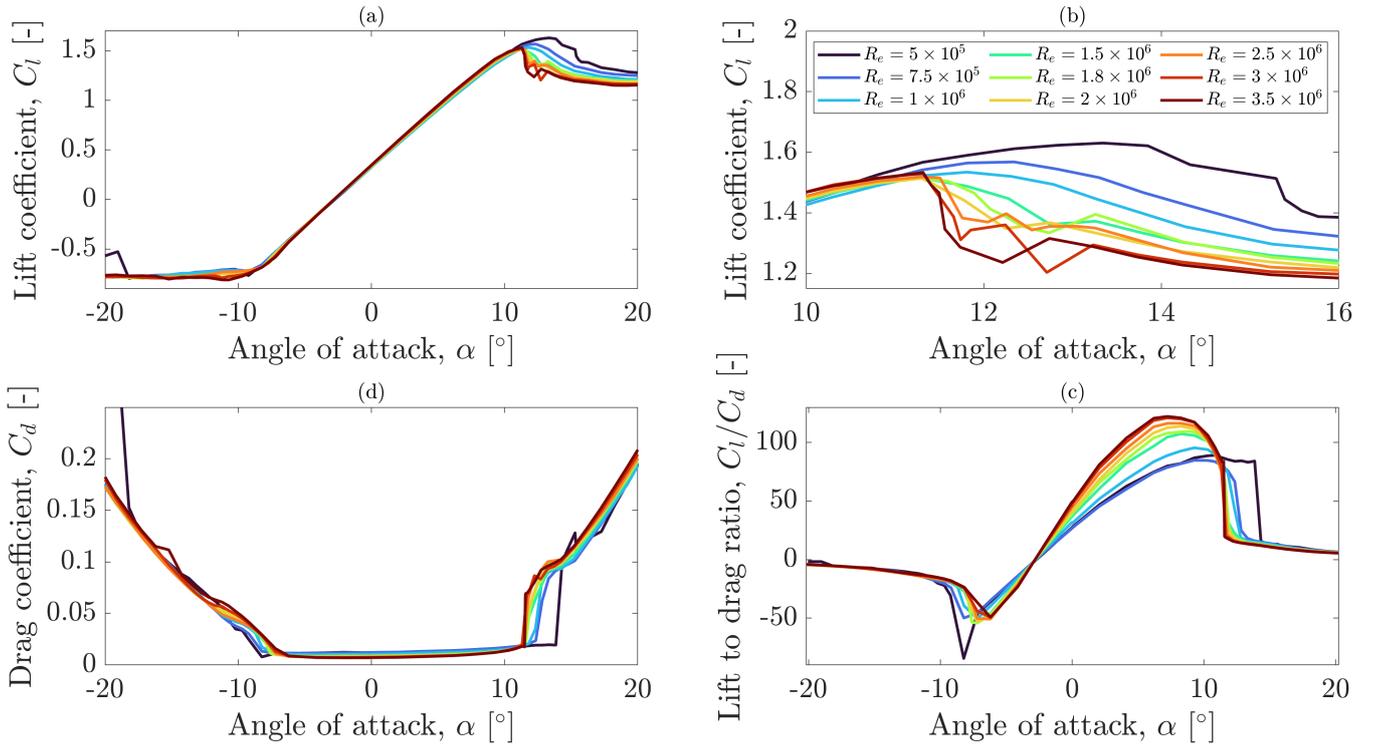
Figure 7. Clean static polars for the FFA-W3-211 for $5 \times 10^5 \leq Re_c \leq 3.5 \times 10^6$.

230   static polars were acquired for $-5.43° < \alpha < 31°$. Finally, results from RFOIL simulations are included (Van Rooij, 1996). The results depicted in Fig. 6 show agreement in both the lift and drag coefficients.

3.2   Static polars

The newly acquired airfoil polars are the starting point for this analysis. Static results are presented in Fig. 7. The slope in the linear region of the lift coefficient curve slightly increases with the Reynolds number. The highest aerodynamic efficiency

235   shows more significant Reynolds number effects. Firstly, the $(C_l/C_d)_{max}$ increases in magnitude with increasing Reynolds numbers. Secondly, the value of α at which the highest aerodynamic efficiency is found decreases with increasing Reynolds numbers. Overall, the aerodynamic efficiency dependens strongly on the Reynolds number, as explained in Ceyhan et al. (2017).

As the Reynolds number increases, the maximum lift coefficient drops, however above $Re_c = 2 \times 10^6$, it increases again. The

240   same kind of regime change was identified in Brunner et al. (2021) for a different airfoil. The angle of attack at which the maximum lift coefficient is found follows a similar trend. At low Reynolds numbers, stall occurs at higher angles of attack. This angle decreases as the Reynolds number increases as a result of a combination of changes in boundary layer thickness
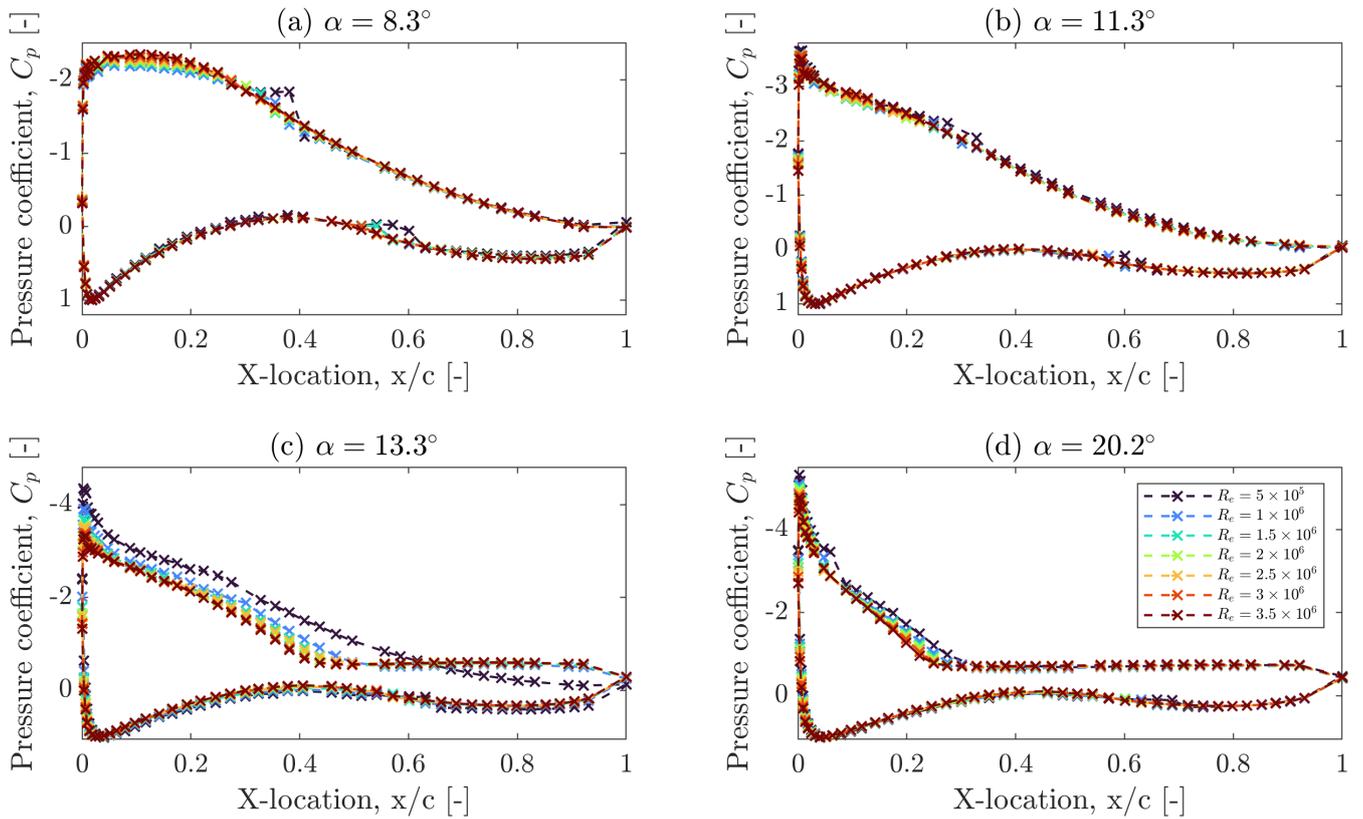
12

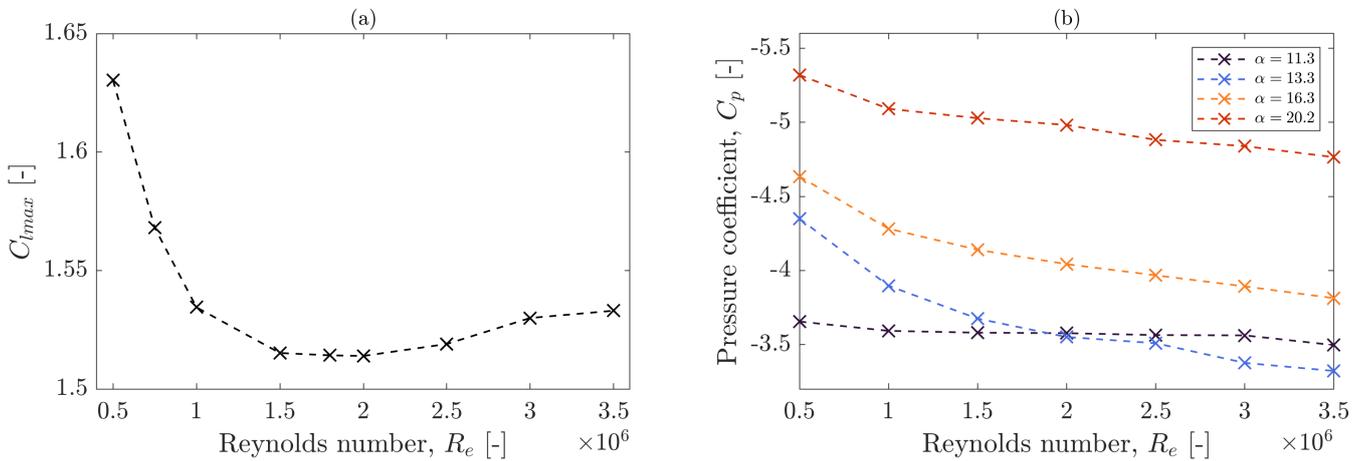**Figure 8.** Pressure contours for relevant angles of attack.

Figure 9. Maximum lift coefficient (a) and suction peak (b) as a function of Reynolds number and angle of attack for the clean airfoil.

and the separation point, but stays roughly constant after $Re_c = 2 \times 10^6$. From the above, we can conclude that two distinct regimes exists that are solely determined by how the polars are impacted by a change in Reynolds number.

245   An explanation for this change in physical behavior could possibly be the presence of a small laminar separation bubble (LSB) for the lower Reynolds numbers that vanishes at the higher Reynolds numbers (also depending on the angle of attack). An indication for this speculation can be found in Fig. 8 (a). Here, for $Re_c = 5 \times 10^5$, a small plateau in the pressure coefficient could be discerned for both the suction and pressure sides at roughly $0.32 < x/c < 0.40$ and $0.47 < x/c < 0.65$, respectively. An increase in Reynolds number (or angle of attack) can move the location of laminar-to-turbulent transition upstream and

250 thus diminish or eliminate the LSB.

     The position and magnitude of the suction peak also change with the Reynolds number. A higher suction peak is first identified for low Reynolds numbers. For the same angle of attack, the x/c position at the highest magnitude slightly shifts towards the trailing edge for increasing Reynolds numbers. The trend is shown in Fig. 9, where the static stall angle is also presented. Here, the magnitude of the suction peak shows Reynolds number effects.

255   The different stall behaviour also highlights the effects of the Reynolds number. The stall behaviour is gradual for the regimes in which an LSB is suspected from the pressure distribution. The stall becomes more abrupt for the highest Reynolds number, in agreement with high-Reynolds literature. The stall behaviour can be classified as a trailing-edge stall for the lowest tested Reynolds numbers. As the Reynolds number increases, the separation point on the suction side moves towards the leading edge. Figure 8 (b) shows the change in stall behaviour, from a smooth transition at lower Reynolds regimes to a more abrupt drop.

260 Figure 8 (c) indicates that for $\alpha = 13.3°$, the flow is only attached for the $Re_c = 5 \times 10^5$ case. Figure 8 (d) displays the effects of the Reynolds number on the location of the separation point, which moves upstream with increasing Reynolds numbers. This is associated with a decreasing suction peak magnitude, $C_{p_{min}}$, as shown in Fig. 9 (b). Figure 9 a shows the Reynolds effects on the maximum lift coefficient. As shown in Brunner et al. (2021) and Kiefer et al. (2022) for a NACA0021, the maximum lift coefficient value is found to increase past $Re_c \approx 2 \times 10^6$. From all of the above, for the FFA-W3-211 airfoil, static experiments of

265 $Re_c = 2 \times 10^6$ or above are recommended to more likely capture correct physical trends relevant for larger wind turbine blades.

3.3   Dynamic polars

The dynamic results are evaluated by isolating (where possible) Reynolds number effects and the response to different reduced frequencies, oscillating frequencies and amplitudes. Note that capturing the large wake shed by the airfoil with a rake for the

270 dynamic cases was not possible. Therefore, the (uncorrected) normal coefficient results are presented and averaged over 50 loops of dynamic stall for all cases. The angles of attack are presented with an accuracy of $\pm 1°$ due to some minor play in the linear actuator motion, particularly found for the highest inertia cases.

3.3.1   Reynolds number effects

The results shown in Fig. 10 (a-c) show the isolated Reynolds number effects on the dynamic normal coefficient for the same

275 reduced frequency. To obtain a constant value of k for the tested Reynolds numbers, a representative oscillating frequency is
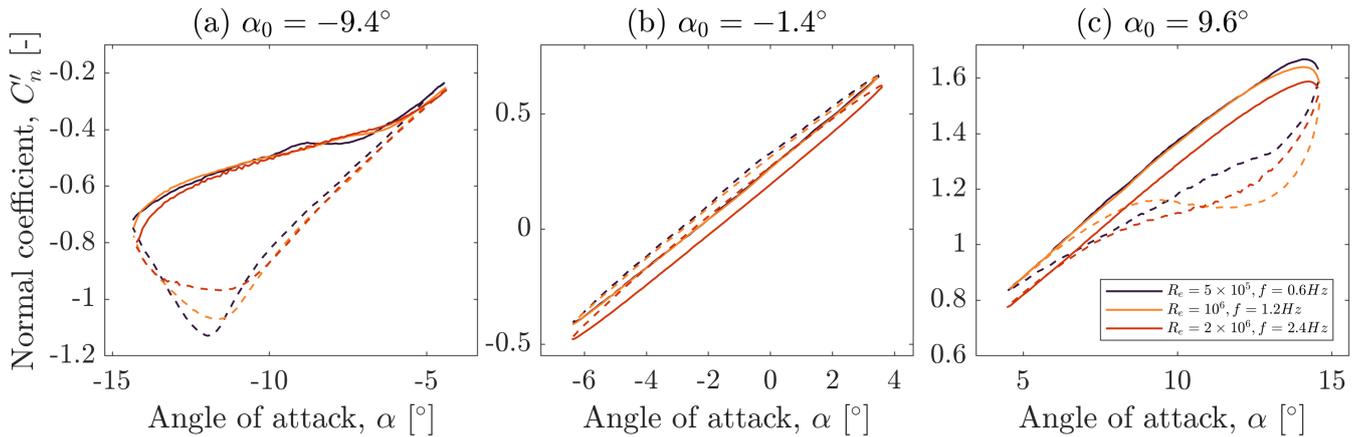
Figure 10. Reynolds number effects for a constant value of $k = 0.091$. The airfoil section is oscillated with an amplitude of $\pm 5°$. The full line represents the upstroke movement, while the dotted line represents the downstroke movement. Data averaged over 50 dynamic stall cycles.

selected. Three mean angles are chosen as the centre of the sinusoidal oscillation in the linear, positive, and negative regions of the polars. It was only possible to test one reduced frequency for all Reynolds numbers due to setup limitations, corresponding to a value of $k = 0.091$ as seen in Tab. 3.

The negative region of the polars is shown in Fig. 10 (a), where the Reynolds number is found to affect the negative stall behaviour, following the same trend as the positive region of the polars in Fig. 10 (c). The trends align with the static data results, where the lowest Reynolds number corresponds to the highest forces. Unlike Fig. 10 (a), the reattachment behaviour is found to be mostly independent of the Reynolds number for the negative region of the polars.

In the linear region, the Reynolds number barely affects the slope and forces magnitude, with all cases showing similar values in both the nose-up and nose-down motions. The hysteresis loop displays the same difference in nose-up and nose-down behaviour.

In the positive regime, higher loads are observed for the lowest Reynolds number, in line with the static results shown in figure 9. The flow reattachment behaviour during the nose down motion is found to exhibit significant differences, where for $Re_c = 5 \times 10^5$ and 2×10^6, the behaviour appears smooth and gradual. For $Re_c = 10^6$, strong reattachment is observed in the data, with an accelerated reattachment behaviour as the airfoil oscillates back into the linear region. As for the static case, for the FFA-W3-211 airfoil, dynamic experiments of $Re_c = 2 \times 10^6$ or above are recommended to better capture the physical trends relevant for larger wind turbine blades.
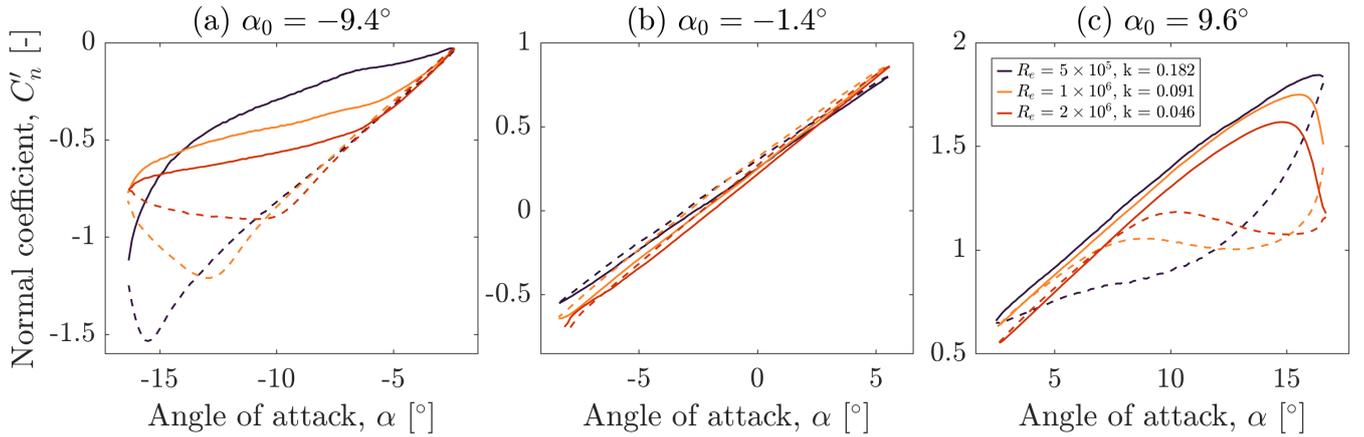
Figure 11. Reduced frequencies and Reynolds numbers effects combined for $f = 1.2Hz, A = 7°$. The reduced frequency range is $k = 0.182, 0.091, 0.046$. The full line represents the upstroke airfoil section movement, while the dotted line represents the downstroke movement. Data averaged over 50 dynamic stall cycles.

Table 3. Reduced frequencies range matrix for the dynamic oscillations. It is possible to compare results from different Reynolds numbers for the same value of $k = 0.091$.

/	$Re_c = 5 \times 10^5$	$Re_c = 10^6$	$Re_c = 2 \times 10^6$
$f = 0.6Hz$	0.091	0.046	0.023
$f = 1.2Hz$	0.182	0.091	0.046
$f = 1.8Hz$	0.273	0.137	0.068
$f = 2.4Hz$	0.365	0.182	0.091

3.3.2 Combined Reynolds number and reduced frequency effects

Together with the Reynolds number, the reduced frequency directly affects the airfoil performance. Given the low Mach number, it is possible to combine the effects of k by varying the oscillating frequency, described in Eq. (4), and Reynolds number. This value falls in the unsteady regime according to Corke and Thomas (2015).

The results are shown in Fig. 11. Firstly, reattachment in the downstroke movement in Fig. 10 (c) exhibits different magnitudes and behaviours as a result of different reduced frequencies. Fig. 10 (a-c) showcased the isolated effects of the Reynolds number, which only affected the dynamic polars in the negative and positive stall and reattachment behaviour. Therefore, the significant stall delay and higher magnitude shown in Fig. 11 (a-c) can be attributed to changing values of k.

For the lowest Reynolds number and frequency, the reattachment is quite linear. As both parameters double, the initial reattachment is faster, with a strong and sudden decrease in loads. In the negative region of the polars, the unsteady effects are visible in the lower minimum normal coefficient attained at higher Reynolds numbers, where higher reduced frequencies are responsible for larger force differences in the nose-down and nose-up motions. The mechanisms that describe the boundary layer attachment are a function of the variation in leading-edge suction peak and trailing-edge stall evolution.

This is due to the higher inertia introduced in the system, at which the reduced frequency decreases and with decreasing free-stream velocity. The normal coefficient magnitude decreases with increasing Reynolds numbers and reduced frequencies to the point where, for highly unsteady reduced frequencies, separation does not take place for angles of attack as high as $\alpha = 16.6°$. The linear region of the polars shows minor differences in magnitude. A difference in slope is found as both parameters are varied, in agreement with previous literature (De Tavernier et al., 2021; Kiefer et al., 2022). The linear region slope is found to increase with decreasing reduced frequencies, independently of the Reynolds number, as shown in the previous section of the manuscript.

Lastly, the negative region of the polars showcases two different reattachment regimes. Here, similarly to the positive region, the highest reduced frequencies keep the boundary layer attached at lower angles of attack. At the end of the oscillation, dynamic stall occurs abruptly, leading to a drastic increase in normal coefficient and a rapid reattachment mechanism, significantly faster than the equivalent at lower reduced frequencies.
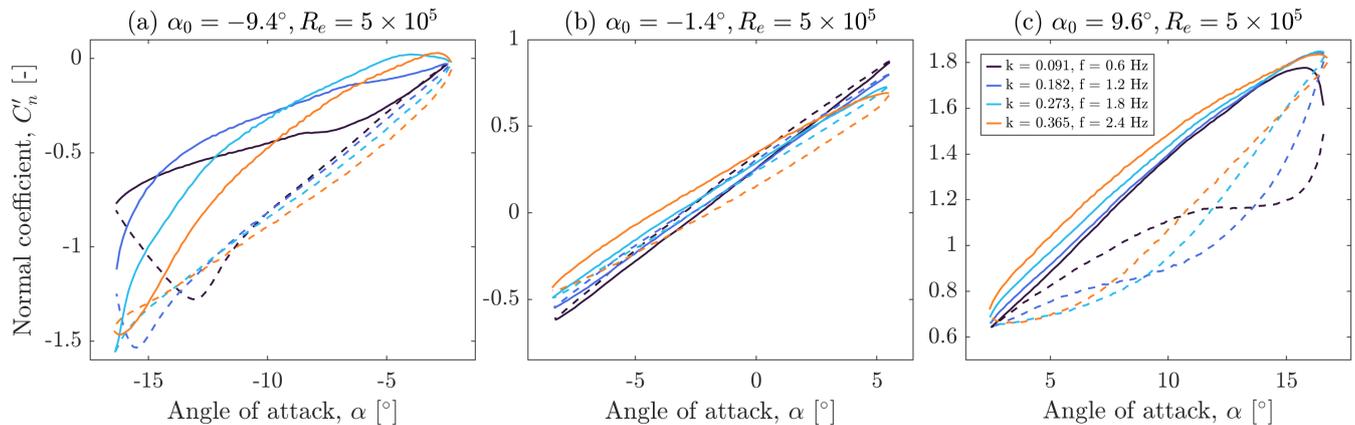
3.3.3 Reduced Frequency effects

Figure 12. Oscillating frequency sweep for $Re_c = 5 \times 10^5, A = 7°$, covering the quasi-steady, unsteady and highly unsteady regimes. The full line represents the upstroke wing movement, while the dotted line represents the downstroke wing movement. Data averaged over 50 dynamic stall cycles.

The effects of varying the oscillating frequency are shown in Fig. 12, 13 and 14, divided by the same mean angle and Reynolds number. The lowest frequency displays a significantly faster reattachment behaviour for all cases tested. For the
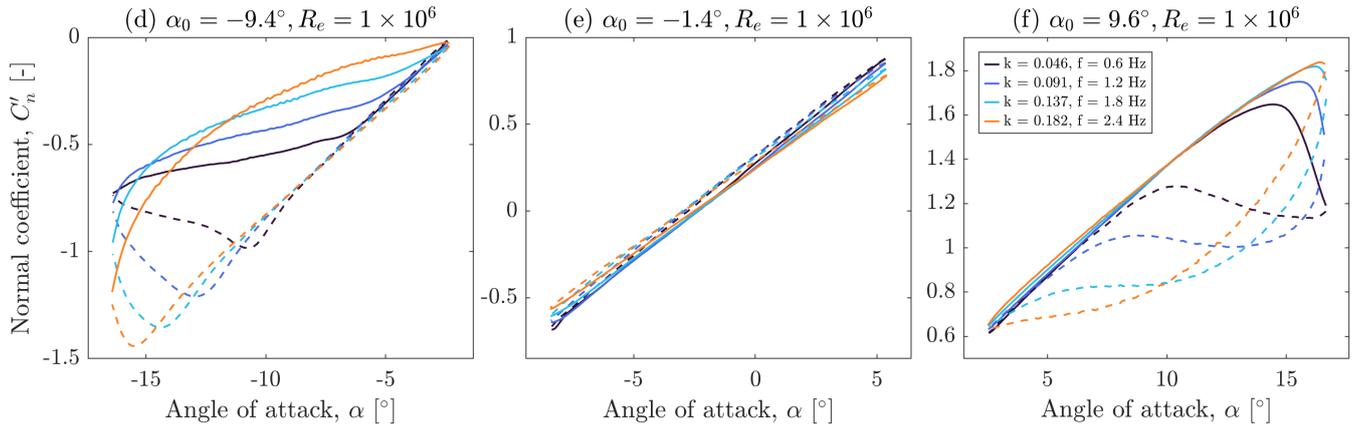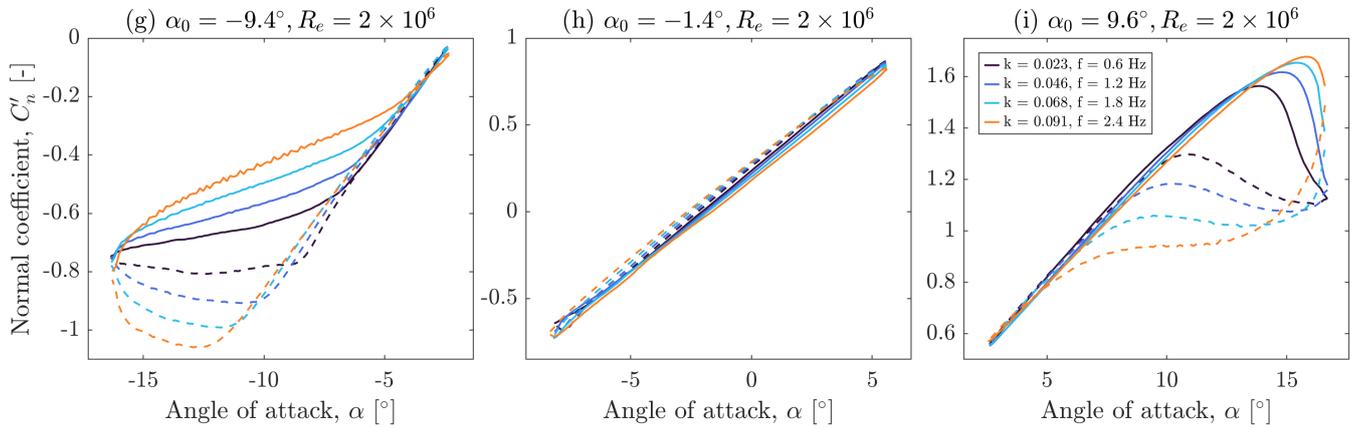
Figure 13. Oscillating frequency sweep for $Re_c = 10^6, A = 7°$, covering the quasi-steady, unsteady and highly unsteady regimes. The full line represents the upstroke wing movement, while the dotted line represents the downstroke wing movement. Data averaged over 50 dynamic stall cycles.

Figure 14. Oscillating frequency sweep for $Re_c = 2 \times 10^6, A = 7°$, covering the quasi-steady, unsteady and highly unsteady regimes. The full line represents the upstroke wing movement, while the dotted line represents the downstroke wing movement. Data averaged over 50 dynamic stall cycles.

lowest reduced frequency of $k = 0.023$, the flow can be considered quasi-steady (Corke and Thomas, 2015), implying that the flow remains attached for slightly more than its static equivalent case. The peak normal coefficient for the positive mean angles is delayed by a few degrees and displays a higher magnitude than the static equivalent, with the value increasing with k for all Reynolds numbers. At the highest reduced frequencies, registered for $Re_c = 5 \times 10^5$, the difference in maximum normal coefficient decreases as the boundary layer remains attached for longer during the upstroke motion. For $k = 0.182, 0.273, 0.365,$
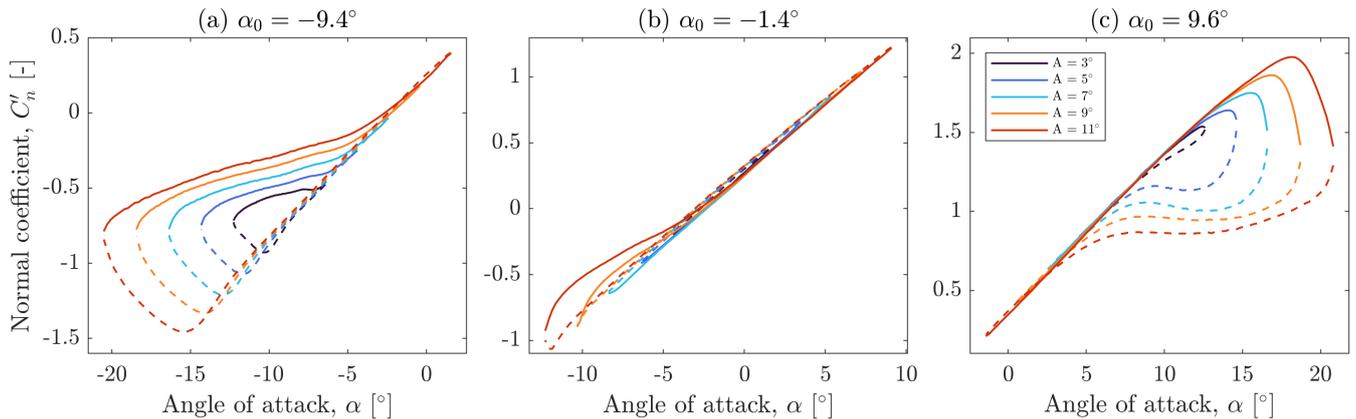
320

18

Figure 15. Amplitude sweep for $Re_c = 1 \times 10^6$, $f = 1.2 Hz$, covering the quasi-steady, unsteady and highly unsteady regimes. The full line represents the upstroke airfoil section movement, while the dotted line represents the downstroke movement. Data averaged over 50 dynamic stall cycles.

no boundary layer separation is observed in the upstroke motion, which reaches $\alpha = 17.6°$. The only case to display separation
325   is at $k = 0.091$, where dynamic stall is observed at $\alpha \approx 15°$.

Reattachment behaviour for the mean positive angle shows good consistency within the same Reynolds number sweep. Both $Re_c = 10^6$ and $Re_c = 2 \times 10^6$ display the same trend where reattachment is fastest at the lowest reduced frequencies. As the reduced frequency increases, the flow remains detached from the airfoil for longer, leading to a higher loss of normal coefficient. Here, for the highest reduced frequency case, the shape of the hysteresis loop almost resembles the one found in the
330   linear region, where the upstroke and downstroke motions showcase greatly different force magnitudes. In general, all reduced frequencies do not converge back to the original linear region slope found at the beginning of the upstroke oscillation, unlike other cases shown in Fig. 13 and Fig. 14. Due to the higher reduced frequencies obtained from the same oscillating frequency value combined with a lower free stream, the $Re_c = 5 \times 10^5$ displays a more unsteady reattachment behaviour.

Finally, the oscillating frequency is found to influence the linear region slope. Here, a Reynolds number dependency is also
335   observed, for which the upstroke and downstroke difference in time-averaged normal coefficient exhibits fewer differences as the Reynolds number increases. Following the conclusions of some high-Reynolds numbers literature (Kiefer et al., 2022), it is expected that the thinner boundary layer will progressively reduce the upstroke and downstroke difference in pressure distribution.

3.3.4   Amplitude effects

340   Results in Fig. 15 display the effects of the oscillating amplitude for a Reynolds number of $Re_c = 10^6$. While pitching the airfoil around the same mean angle, it is immediately visible how, for the positive and negative regions of the polars, the dynamic loop shape is similar between all cases and changes linearly with the angle of attack. For the linear region case,

the highest oscillations can already capture the effects of dynamic stall in the lower regime, showing a difference in normal coefficient for the same angle of attack. This is particularly visible for the $A = 11°$ case, where the oscillation is large enough to capture the dynamic stall cycle. As expected, there are differences between the positive and negative regions of the polars due to the airfoil's camber. Due to the cambered nature of the FFA-W3-211 airfoil, a larger dynamic stall loop is associated with the negative region of the polars where the convergence to the linear region is slow and displays greater discrepancies in the force magnitude. One example is the flow reattachment behaviour, which is observed to be linear in the negative region, while this exhibits a force increase in the positive region.

3.4 Dynamic pressure distribution

Similar to the static counterpart, the dynamic pressure coefficient was retrieved through the pressure taps. Given the airfoil oscillation, these were averaged for an instantaneous angle of attack with a tolerance of $\pm 0.1°$. A number of taps were excluded from the analysis as these were found to be partially blocked, slow or unplugged. As a result, the following plots are obtained from a pressure distribution of 83 pressure taps.
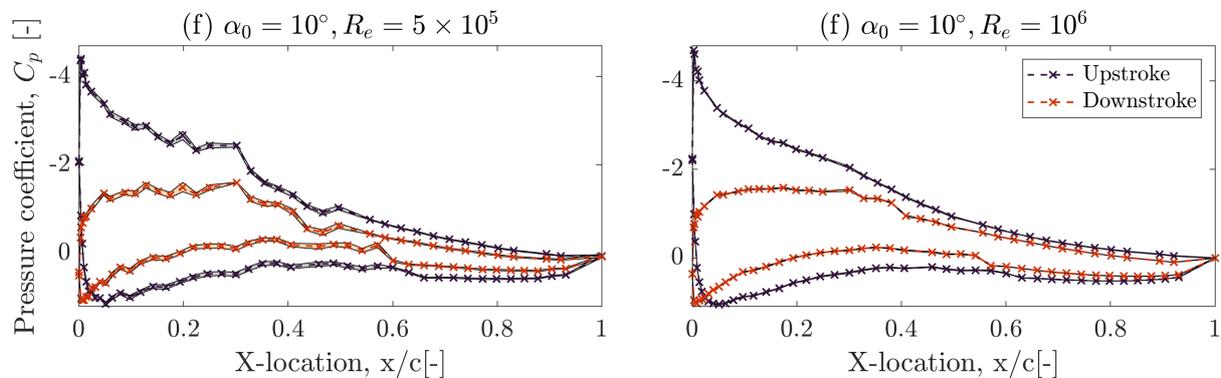

Figure 16. Pressure coefficient standard deviation computed for $A = 7°$, f = $1.2Hz$

In Fig. 17, results are presented for angle of attack of $\alpha = -13°$ and $\alpha = 14°$. Due to the pressure scanner range, the average pressure distribution exhibits a lower resolution at low Reynolds numbers (see Fig. 16).

As the Reynolds number increases, the data appears smoother, also thanks to the decreasing frequency (Fig. 17). Particularly at the lower Reynolds numbers, the discrepancies in the pressure are significant, making it hard to distinguish a LSB. Here, the pressure distributions hint towards the presence of an LSB, particularly supported by the fact that the x/c position is consistent with the static (simulated) data for a Reynolds number of $Re_c = 10^6$, as shown in Fig. 16. It can be noted that the pressure distribution values are not identical and vary significantly for the upstroke and downstroke motions, as suggested in previous plots. The negative values of pressure distribution showcase a clear suction peak in the downstroke motion, which collapses as the airfoil is pitched up. Similar to the static case, this depends on the Reynolds number and reduced frequency combination, and it collapses as the Reynolds number increases. This is partially mitigated by the reduced frequency term. As
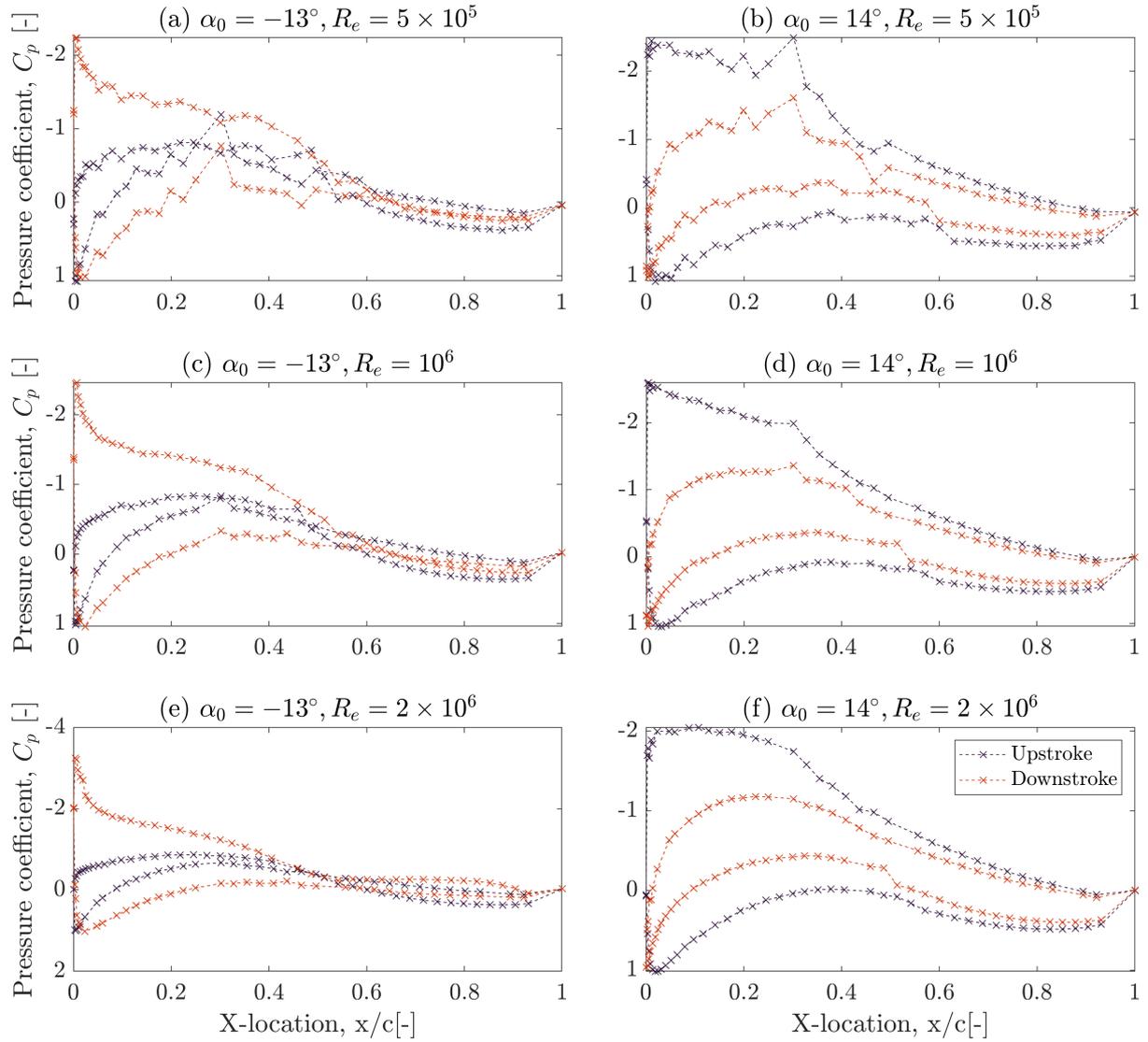
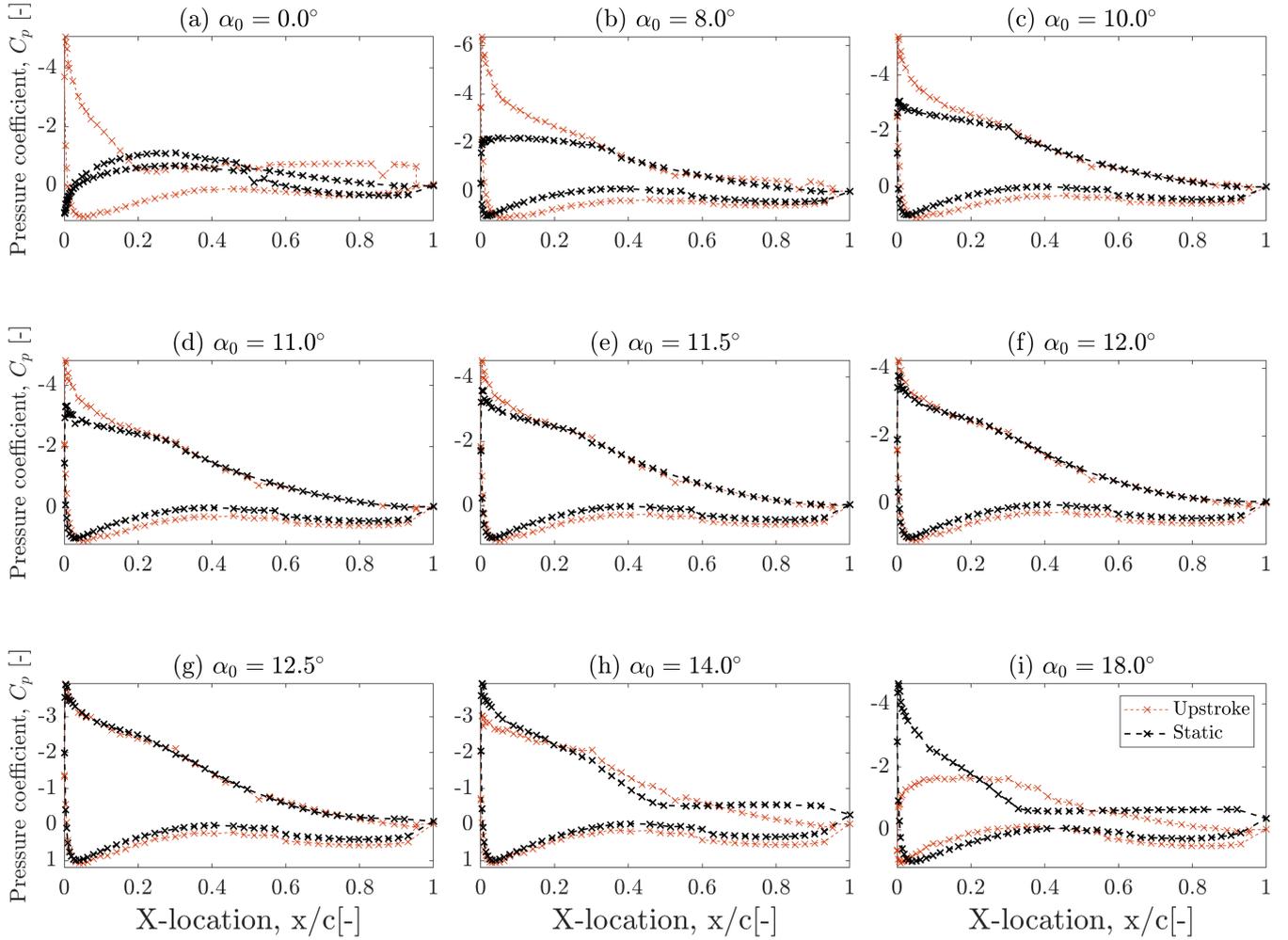**Figure 17.** Dynamic pressure coefficient for $A = 7°$, f = $1.2Hz$

Figure 18. Static and dynamic pressure coefficient comparison for positive angles, $Re_c = 10^6$, f = $1.2Hz$. At $\alpha = 18°$, the trailing edge still displays attached flow during the upstroke oscillation.

365   the flow reattaches, the trailing edge provides the lift, which presents the highest pressure difference. The hysteresis loop is caused by the unsteady flow effects. In the deep dynamic stall conditions, unsteady effects are predominant, with higher force values obtained at higher angles of attack. As highlighted in Kiefer et al. (2022),two mechanisms are responsible for the load development. This is driven by the increase in suction peak magnitude near the leading edge and the boundary layer separation mechanisms originating at the trailing edge. The magnitude variation of the suction peak is responsible for the lift increase. In

370   Fig. 18, a comparison between the static and dynamic pressure distribution is drawn for the same Reynolds number. It can be readily noted that, for $\alpha = 14°$, the static data shows a stalled trailing edge, while the upstroke dynamic data still showcases an attached flow behaviour. This is followed by abrupt dynamic stall at $\alpha = 18°$, where the dynamic suction peak collapses. Overall, the pressure distribution results show good agreement around the static stall region, despite the higher dynamic suction peak for the pre-stall angles of attack.

375   4   Conclusions

This work describes the experimental aerodynamic characterisation of the FFA-W3-211 airfoil. The wind energy community widely uses this airfoil as a popular reference. An experiment was performed in the low-speed, low-turbulence wind tunnel at Delft University of Technology, for which a new airfoil section model with a chord length of $c = 600mm$ and height of $h = 1246mm$ was manufactured. Previously, several wing geometries have been tested in this facility. The airfoil section

380   was pitched sinusoidally in time around its quarter-chord line to acquire the first dynamic data for the airfoil geometry for chord-based Reynolds numbers of up to $Re_c = 2 \times 10^6$.

     The static data suggest the presence of a laminar separation bubble that disappears with increasing Reynolds numbers. Such a flow feature could be responsible for the observed shift in maximum lift trends and static stall behaviour observed around $Re_c = 2 \times 10^6$. The dynamic results display the effects of individual variations in inflow and oscillating parameters. The

385   reduced frequency and Reynolds number effects were described, highlighting their influence on dynamic stall, reattachment and hysteresis loops. For increasing amplitudes, the shape of the hysteresis loop was maintained, but the magnitude increased. This allows for a simple empirical model to capture this effect. The upstroke and downstroke pressure distributions showcase fundamental differences in flow-structure development, ultimately affecting the overall force balance.

     From the findings reported here, it is recommended to use experimental data of $Re_c = 2 \times 10^6$ or above in simulations

390   and model validation or tuning to capture the correct physical (static and dynamic) trends of the FFA-W3-211 airfoil relevant for larger wind turbine blades. For dynamic stall model tuning, it may also be important to consider the significant change in behavior between positive and negative stall angles. Experiments at higher Reynolds numbers than possible for this study would be highly valuable to confirm whether the $Re_c = 2 \times 10^6$ threshold is sufficient. It is also important to bear in mind that the airfoil shape and roughness also plays an important role.

Appendix A

An initial shift of $\alpha = 1.4°$ was observed in the dynamic data. As a result, a calibration was carried out against both static and dynamic ultra-low frequency data. This has allowed to quantify the shift, which is consistent for most cases for $Re_c = 5 \times 10^5, 10^6$ and the negative mean angles for $Re_c = 2 \times 10^6$. However, in some occasions, the data shift observed in the positive regime for the highest Reynolds number shows some irregularities which fall in the $\pm 1°$ regime. This has to be assumed as the reported experimental error for the pitching airfoil cases.
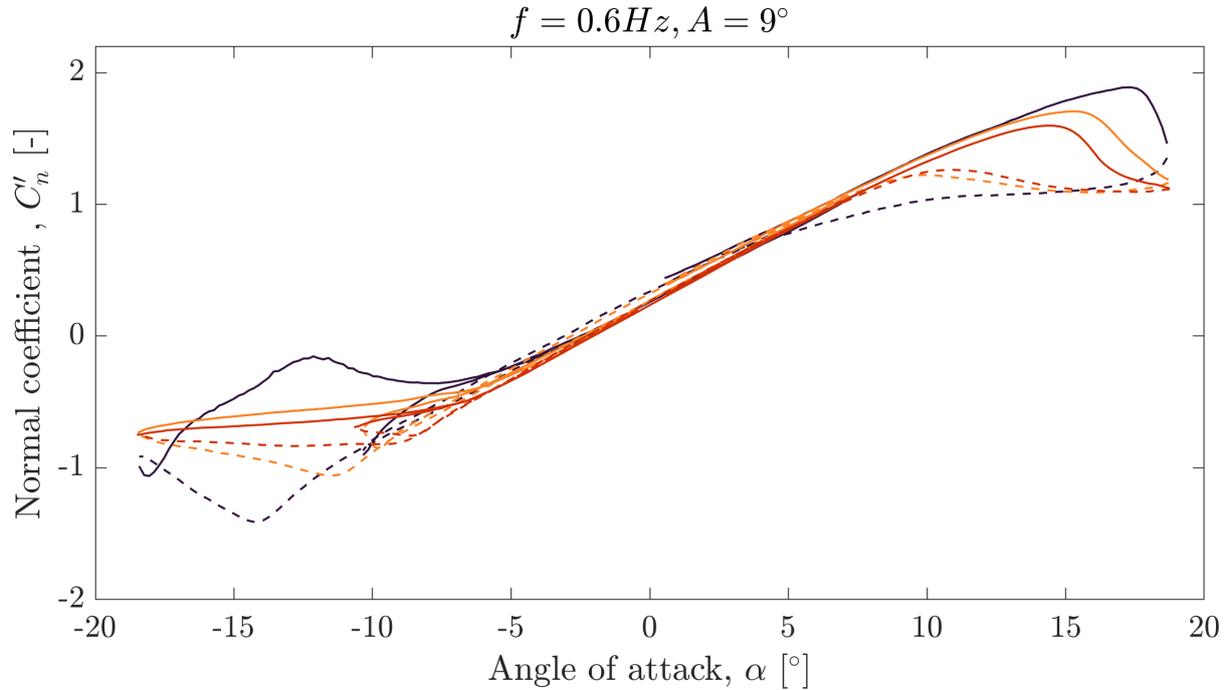

Figure A1. Data overlap between the negative, mean and positive regimes for $A = 9°$, f = $0.6Hz$.

References

Baldacchino, D., Ferreira, C., Tavernier, D. D., Timmer, W., and Van Bussel, G.: Experimental parameter study for passive vortex generators on a 30% thick airfoil, Wind Energy, 21, 745–765, 2018.

Bergh, H. and Tijdeman, H.: Theoretical and experimental results for the dynamic response of pressure measuring systems, 1965.

Bertagnolio, F., Sørensen, N., Johansen, J., and Fuglsang, P.: Wind turbine airfoil catalogue, 2001.

Boutet, J., Dimitriadis, G., and Amandolese, X.: A modified Leishman–Beddoes model for airfoil sections undergoing dynamic stall at low Reynolds numbers, Journal of Fluids and Structures, 93, 102 852, 2020.

Boye, T. and Xie, Z.-T.: Aerodynamics of a pitching wind turbine blade at high reduced frequencies, Journal of Wind Engineering and Industrial Aerodynamics, 223, 104 935, 2022.

Brunner, C. E., Kiefer, J., Hansen, M. O., and Hultmark, M.: Study of Reynolds number effects on the aerodynamics of a moderately thick airfoil using a high-pressure wind tunnel, Experiments in Fluids, 62, 1–17, 2021.

Carta, F. O.: Analysis of oscillatory pressure data including dynamic stall effects, Tech. rep., NASA, 1974.

Ceyhan, O., Pires, O., Munduate, X., Sorensen, N. N., Schaffarczyk, A. P., Reichstein, T., Diakakis, K., Papadakis, G., Daniele, E., Schwarz, M., et al.: Summary of the blind test campaign to predict the high Reynolds number performance of DU00-W-210 airfoil, in: 35th Wind Energy Symposium, p. 0915, 2017.

Chellini, S., De Tavenier, D., and Von Terzi, D.: Impact of dynamic stall model tailoring on wind turbine loads and performance prediction, in: Journal of Physics: Conference Series, vol. 2767, p. 022016, IOP Publishing, 2024.

Choudhuri, P. G. and Knight, D.: Effects of compressibility, pitch rate, and Reynolds number on unsteady incipient leading-edge boundary layer separation over a pitching airfoil, Journal of Fluid Mechanics, 308, 195–217, 1996.

Corke, T. C. and Thomas, F. O.: Dynamic stall in pitching airfoils: aerodynamic damping and compressibility effects, Annual Review of Fluid Mechanics, 47, 479–505, 2015.

Dalton, C.: Allen and Vincenti blockage corrections in a wind tunnel, AIAA Journal, 9, 1864–1865, 1971.

De Tavernier, D., Ferreira, C., Viré, A., LeBlanc, B., and Bernardy, S.: Controlling dynamic stall using vortex generators on a wind turbine airfoil, Renewable Energy, 172, 1194–1211, 2021.

Delft: Low turbulence tunnel, https://www.tudelft.nl, accessed: 18/09/2023, 2017.

Gaertner, E., Rinker, J., Sethuraman, L., Zahle, F., Anderson, B., Barter, G., Abbas, N., Meng, F., Bortolotti, P., Skrzypinski, W., et al.: Definition of the IEA 15-megawatt offshore reference wind turbine, 2020.

Gardner, A. D., Jones, A. R., Mulleners, K., Naughton, J. W., and Smith, M. J.: Review of rotating wing dynamic stall: Experiments and flow control, Progress in Aerospace Sciences, 137, 100 887, 2023.

Gharali, K. and Johnson, D. A.: Dynamic stall simulation of a pitching airfoil under unsteady freestream velocity, Journal of Fluids and Structures, 42, 228–244, 2013.

Ham, N. D.: Stall flutter of helicopter rotor blades: a special case of the dynamic stall phenomenon, Journal of the American Helicopter Society, 12, 19–21, 1967.

Kiefer, J., Brunner, C. E., Hansen, M. O., and Hultmark, M.: Dynamic stall at high Reynolds numbers induced by ramp-type pitching motions, Journal of Fluid Mechanics, 938, A10, 2022.

Leishman, J.: Dynamic stall experiments on the NACA 23012 aerofoil, Experiments in Fluids, 9, 49–58, 1990.

Leishman, J. G.: Challenges in modelling the unsteady aerodynamics of wind turbines, Wind Energy: An International Journal for Progress and Applications in Wind Power Conversion Technology, 5, 85–132, 2002.

Leishman, J. G. and Beddoes, T.: A Semi-Empirical model for dynamic stall, Journal of the American Helicopter society, 34, 3–17, 1989.

Llorente, E., Gorostidi, A., Jacobs, M., Timmer, W., Munduate, X., and Pires, O.: Wind tunnel tests of wind turbine airfoils at high Reynolds numbers, in: Journal of Physics: Conference Series, vol. 524, p. 012012, IOP Publishing, 2014.

McAlister, K. W., Carr, L. W., and McCroskey, W. J.: Dynamic stall experiments on the NACA 0012 airfoil, Tech. rep., 1978.

McAlister, K. W., Lambert, O., and Petot, D.: Application of the ONERA model of dynamic stall, Tech. rep., 1984.

McCroskey, W. J.: Unsteady airfoils, 1982.

Melani, P., Aryan, N., Greco, L., and Bianchini, A.: The Beddoes-Leishman dynamic stall model: Critical aspects in implementation and calibration, Renewable and Sustainable Energy Reviews, 202, 114 677, 2024.

Øye, S.: Dynamic stall simulated as time lag of separation, in: Proceedings of the 4th IEA Symposium on the Aerodynamics of Wind Turbines, vol. 27, p. 28, Rome, Italy, 1991.

Patterson, M. and Lorber, P.: Computational and experimental studies of compressible dynamic stall, Journal of fluids and structures, 4, 259–285, 1990.

Rainbird, J. M., Bianchini, A., Balduzzi, F., Peiró, J., Graham, J. M. R., Ferrara, G., and Ferrari, L.: On the influence of virtual camber effect on airfoil polars for use in simulations of Darrieus wind turbines, Energy Conversion and Management, 106, 373–384, 2015.

Snel, H.: Heuristic modelling of dynamic stall characteristics, in: EWEC-conference-, pp. 429–433, Bookshop for Scientific Publications, 1997.

Stettner, M., Reijerkerk, M. J., L√°nenschlo√ü, A., Riziotis, V., Croce, A., Sartori, L., Riva, R., and Peeringa, J. M.: Stall-Induced Vibrations of the AVATAR Rotor Blade, Journal of Physics: Conference Series, 753, 042 019, https://doi.org/10.1088/1742-6596/753/4/042019, 2016.

Timmer, W. and Van Rooij, R.: Summary of the Delft University wind turbine dedicated airfoils, J. Sol. Energy Eng., 125, 488–496, 2003.

Tuncer, I. H., Wu, J. C., and Wang, C.: Theoretical and numerical studies of oscillating airfoils, AIAA journal, 28, 1615–1624, 1990.

Van Rooij, R.: Modification of the boundary layer calculation in RFOIL for improved airfoil stall prediction, 1996.

Zahle, F., Barlas, T., Lonbaek, K., Bortolotti, P., Zalkind, D., Wang, L., Labuschagne, C., Sethuraman, L., and Barter, G.: Definition of the iea wind 22-megawatt offshore reference wind turbine, Tech. rep., National Renewable Energy Laboratory (NREL), Golden, CO (United States), 2024.